Chemical Engineering Journal 342 (2018) 339–349

Contents lists available at ScienceDirect

Chemical Engineering Journal

journal homepage: www.elsevier.com/locate/cej

Simultaneous removal of NO and Hg^0 from simulated flue gas over CoO_x-CeO_2 loaded biomass activated carbon derived from maize straw at low temperatures

Lei Gao[a,b], Caiting Li[a,b,*], Jie Zhang[a,b], Xueyu Du[a,b], Shanhong Li[a,b], Jiawen Zeng[a,b], Yaoyao Yi[a,b], Guangming Zeng[a,b]

[a] *College of Environmental Science and Engineering, Hunan University, Changsha 410082, PR China*
[b] *Key Laboratory of Environmental Biology and Pollution Control (Hunan University), Ministry of Education, Changsha 410082, PR China*

HIGHLIGHTS

- Manufacturing maize straw derived BAC obtains the unit of environmental and economic benefits.
- $15\%Co_{0.4}Ce_{0.6}/BAC$ exhibited superior performance for simultaneous removal of NO and Hg^0.
- The interaction between NO reduction and Hg^0 oxidation was investigated.
- The mechanisms of simultaneous removal of NO and Hg^0 were systematically proposed.

GRAPHICAL ABSTRACT

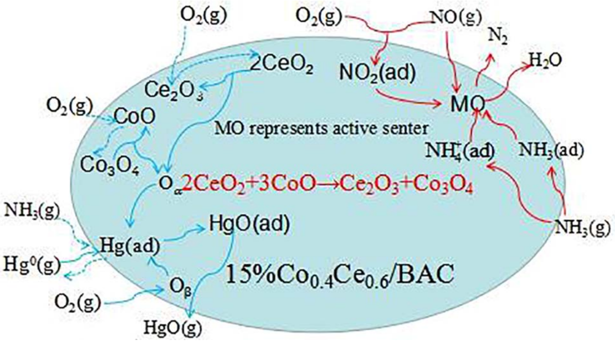

ARTICLE INFO

Keywords:
Simultaneous removal
NO
Elemental mercury
CoCe/BAC
Adsorption
Catalytic oxidation

ABSTRACT

To rationally utilize agricultural wastes and expediently simultaneous control of elemental mercury (Hg^0) and NO, a series of CoO_x-CeO_2 loaded maize straw derived biomass activated carbon (CoCe/BAC) samples were applied for simultaneous NO and Hg^0 removal. These samples' physicochemical characteristics were characterized by BET, SEM, XRD, NH_3-TPD, H_2-TPR, XPS and FTIR. $15\%Co_{0.4}Ce_{0.6}/BAC$ yielded prominent Hg^0 removal efficiency (96.8%) and superior NO removal efficiency (84.7%) at 230 °C. The separate or synchronous deactivation effects of 400 ppm SO_2 and $5\%H_2O$ were detected. The interaction between NO removal and Hg^0 removal was investigated, the results demonstrated that abundant Hg^0 exhibited very slightly inhibitory effect on NO removal, and NH_3 negatively affected Hg^0 removal, whereas NO mildly boosted Hg^0 removal in presence of O_2. The characterization analyses indicated the excellent performance of $15\%Co_{0.4}Ce_{0.6}/BAC$ could be ascribed to its better texture properties, lower crystallinity and stronger redox ability. Besides, a synergetic effect appeared between cobalt oxide and cerium oxide, resulting in generating more Ce^{3+} and Co^{3+} to induce more anionic defects and produce more active oxygen and oxygen vacancies. The removal mechanisms of NO and Hg^0 were systematically investigated, and NO reduction reactions were mainly assigned to the Langmuir-Hinshlwood mechanism while both adsorption and Hg^0 oxidation contributed to Hg^0 removal. Meanwhile, Hg^0 oxidation corresponded to the Mars-Masson mechanism prevailed gradually with the increase of reaction time.

---

* Corresponding author at: College of Environmental Science and Engineering, Hunan University, Changsha 410082, PR China.
E-mail address: ctli@hnu.edu.cn (C. Li).

https://doi.org/10.1016/j.cej.2018.02.100
Received 5 December 2017; Received in revised form 19 February 2018; Accepted 23 February 2018

1. Introduction

Coal-fired power plant, as the major contribution of worldwide energy demand, has become one of leading anthropogenic atmosphere pollutant emission sources [1–3]. Thereinto, nitrogen oxides (NO_x) and elemental mercury (Hg^0) are deemed to be two significant atmosphere pollutants and have aroused widespread concern. NO_x is considered as an incentive for numerous environmental problems, such as regional acid smog, zone depletion and photochemical smog [3]. Hg^0 is a global threat to the environment and human health because of its volatility, toxicity, persistence and bioaccumulation [2,3]. Consequently, more and more national laws and regulations have been implemented to restrict NO_x and Hg^0 emissions [4,5]. For example, some strict regulations aiming to achieve ultra low emission in coal-fired power plants are put forward in China, in which the emission concentrations of NO_x and Hg^0 are limited to 5 mg/m^3 and 0.002 mg/m^3, respectively [5].

Therefore, enormous technologies have been developed to reduce NO_x or Hg^0 emissions from coal-fired power plants to meet these laws and regulations [2,4–6]. Among them, selective catalytic reduction (SCR) of NO_x with NH_3 is regarded as one widely applied technique due to its excellent performance, while activated carbon injection (ACI) for Hg removal has been a mature technology [2,7]. However, the ACI technology suffers from many shortcomings such as the low capture efficiency at high temperature, potential secondary pollution caused by spent sorbents and high operating cost due to the tremendous consumption of activated carbon (AC) [8,9]. Moreover, traditionally separate NO_x and Hg^0 control technology faced several bottlenecks including large footprint requirement, high equipment and operation investment [10]. Hence, it is easy to consider whether or not to utilize the denitration catalyst for Hg^0 removal, but researches demonstrated the most widely engaged denitrification catalysts (V_2O_5-WO_3(MoO_3)/TiO_2) were not effective enough for Hg^0 conversion in the flue gas burnt the low chlorine coal [4,6]. Furthermore, to avoid deactivation and reduce reaction costs, the SCR system was required to be loaded downstream of the particulate collector where the temperature was lower than the narrow active temperature window of the for-mentioned SCR catalyst [6,11]. Considering these handicaps, the development of novel appropriate catalysts for simultaneous removal NO_x and Hg^0 at low temperature is of significantly practical interest.

Up to date, CeO_2 has been successfully widely used in a variety of heterogeneous reactions as an effective catalyst, a promoter, a support or active ingredient for NO reduction and Hg^0 oxidation respectively because of its large oxygen storage capacity and unique redox couple Ce^{4+}/Ce^{3+} [4,12–14]. It was known that the combination of CeO_2 with other metal oxides such as MnO_x, CuO and La_2O_3 could produce synergistic effect, which was conducive to the promotion of NO reduction and Hg^0 oxidation [4,6,15,16]. Zhang et al. [17] studied hollow porous $Mn_xCo_{3-x}O_4$ nanocages deNO_x catalyst and found it had excellent low temperature activity and good SO_2 resistance. Due to the synergistic effect of high oxygen storage-release ceria and active Co species, Co_3O_4–CeO_2 composite catalyst, Co_3O_4/CeO_2 catalyst and CoO_x-CeO_2 loaded activated coke sorbent-catalyst had been reported to yield superior performance for VOCs oxidation [18,19], CO oxidation [20] and Hg^0 oxidation [14], respectively. However, to the authors' knowledge, systematic researches with respect to CoO_x and CeO_2 as active ingredients for NO_x and Hg^0 simultaneous removal are rarely reported.

In addition, activation carbon (AC) is considered as the most widely employed sorbent and the carrier of catalysts due to its large surface areas, favorable pore size and flexible working conditions [6,14,21]. Traditional ACs are usually derived from relatively expensive and non-renewable raw materials such as bituminous coal and wood. At the same time, as a big agricultural country, China faces the challenges from the dispose of billions of tons of renewable agriculture straws every year. Since most of them cannot receive reasonable utilization and be open burning, thus engendering great harms to the environment [22]. Therefore, it is much monetary and environmentally friendly incentive for manufacturing biomass activated carbon (BAC) derived from annually renewable agriculture wastes. Thus, biomass activated carbons (BAC) derived from agriculture wastes have become a new concern due to significant practical interest [23,24]. Nevertheless, these BACs are mainly used for waste water treatment [23], and only limited applications on gas purification [24]. Notably, some meaningful researches related to bio-chars from various straws have emerged for mercury removal by adsorption or catalytic oxidation [25,26]. However, as we know, ideal adsorbents/catalysts should possess excellent surface area, these bio-chars often own unimpressive BET surface areas (about 200 m^2/g). In this work, BACs from maize straw prepared by $ZnCl_2$ activation have severalfold BET surface areas (543–1029 m^2/g), which are more propitious to adsorption and catalytic reactions. CoO_x and CeO_2 supported on the carrier of BAC by the impregnation method were investigated for NO and Hg^0 simultaneous removal.

2. Experimental

2.1. Preparation of samples

Maize straws were collected from the rural areas of Xinyang city, Henan province, PR China. The raw material was first rinsed with deionized water and dried at 105 °C overnight, crushed and sieved for standby application. Then the resulted particles (RP) were impregnated into $ZnCl_2$ solution at calculated quantity (the mass ratio of activating agent ($ZnCl_2$) and RP of 1, which was chosen based on our preliminary experiments) for 24 h at ambient temperature. After that, the obtained materials were dried at 105 °C overnight, and subsequently they were activated in a tube-type electronic heating furnace at 750 °C for 2 h under N_2. After activation, the obtained materials were washed several times by 5 M HNO_3 and then bathed with deionized water until the pH of cleaning water reached approximately 7. Subsequently, the product was dried and sieved, thus obtaining the carrier of BAC.

The catalysts were prepared by impregnation method using foregoing BAC as the carrier and cobalt nitrate or cerium nitrate as the precursors of active ingredients. Calculated amounts of BACs were impregnated in corresponding precursors solutions for 24 h. Afterwards, these impregnated samples were dried at 105 °C for 18 h and then calcined at 550 °C for 4.5 h under N_2 atmosphere. Thus XCo_yCe_{1-y}/BAC catalyst was obtained, where X represented the mass percentage of metal oxides of the Co_y Ce_{1-y}/BAC samples while y referred to the molar ratio of Co in metal oxides, similarly, 1-y referred to the molar ratio of Ce in metal oxides. Moreover, for comparison, XCo/BAC and XCe/BAC were synthesized by the same method.

2.2. Sample characterization

Pore characteristics including average pore diameter, total pore volume and Brunauer–Emmett–Teller (BET) surface area of different samples were acquired by N_2 adsorption with an automatic Micromeritics ASAP2460 volumetric sorption analyzer (Micromeritics Instrument Corp., USA).

The microstructure and morphology of different samples were measured by Scanning electron microscopy (SEM) using Nova Nano SEM 230 (USA).

X-ray diffraction (XRD) measurements of different samples were carried out on a Rigaku Smartlab (3KW) system (Japan) with Cu-Ka radiation (40 kV, 30 mA) in the 2θ range from 10° to 90°.

H_2-temperature programmed reduction (H_2-TPR) and ammonia-temperature programmed desorption (NH_3-TPD) were conducted on a TP-5080 automatic chemical adsorption instrument (Tianjin Xianquan, China).

X-ray photoelectron spectroscopy (XPS) was performed using a K-Alpha 1063 X-ray photoelectron spectrometer with 72 W Al Kα radiation (Thermo Fisher Scientific, USA).

Fourier transform infrared spectroscopy (FTIR) was conducted on a

FTIR IRInfinity-1 spectrometer to investigate the surface groups of samples (Shimadzu, Japan). Its special region was between 4000 and 400 cm^{-1} with a 2 cm^{-1} resolution. Prior to the measurement, each sample was pretreated at 300 °C for 2 h to remove possible adsorbed species. Afterwards, the adsorption test was conducted for 1 h with a total gas flow of 500 mL/min at ambient temperature.

2.3. Sample activity test

The experimental schematic diagram was provided in our previous works [27,28]. The simulated flue gas (SFG) contained 100 μg/m^3 Hg^0(g), 6% O_2, 600 ppm NO, 600 ppm NH_3 and N_2 as the carrier gas and balance gas. Other concentrations of NO, NH_3, O_2 and Hg^0(g) as well as SO_2, H_2O(g) were provided when needed. N_2, O_2, NO, NH_3 and SO_2 from cylinder gases were accurately controlled by mass flow controllers, whereas the generation and control of certain concentrations of Hg^0(g) or H_2O (g) were described detailedly in our previous works [6,14]. Prior to each test, these gases mixed with each other in a gas mixing bottle. The total flow rate was maintained at 500 mL/min in all experiments and 300 mg sample corresponded to a space velocity of approximately 100,000 h^{-1} was laid in the central part of a quartz tube with an inner diameter of 10 mm and a length of 600 mm. The concentrations of NO and Hg^0 were measured by an on-line mercury analyzer (Lumex RA-915 M, Russia, detection limit = 2 ng/m^3) with a data acquisition computer and a flue gas analyzer (MGA5, Germany).

Before the activity test, the blank test of the system was conducted and the effects of the pipes and the reactor on NO and Hg^0 removal were proved to be negligible. In addition, a mercury conversion test was conducted to confirm mercury speciation as our previous works [6,21,29]. In which gas released from the reactor was firstly divided into two branches, one went to 10% KCl aqueous solution to remove Hg^{2+} for Hg^0 measurement, and the other went to 10% $SnCl_2$ aqueous solution to reduce Hg^{2+} to Hg^0 for total elemental mercury ($Hg_{out}^{0\ T}$) measurement. Then they went through 10% NaOH aqueous solution to remove acidic gas in the front of the mercury analyzer. The definition of NO removal efficiency (E_{NO}) and Hg^0 removal efficiency (E_{Hg}) were given below by Eq. (1) and Eq. (2), respectively. Thence, the oxidation efficiency of Hg^0 (Eoxi) could be calculated by Eq. (3).

$$E_{NO} = \frac{NO_{in} - NO_{out}}{NO_{in}} \times 100\% \tag{1}$$

$$E_{Hg} = \frac{Hg_{in}^{0} - Hg_{out}^{0}}{Hg_{in}^{0}} \times 100\% \tag{2}$$

$$E_{oxi} = \frac{Hg_{out}^{0\ T} - Hg_{out}^{0}}{Hg_{in}^{0}} \times 100\% \tag{3}$$

where NO_{in} and NO_{out} represent the inlet NO concentration and the outlet NO concentration, respectively. Similarly, Hg_{in}^0 and Hg_{out}^0 denote the inlet Hg^0 concentration and the outlet Hg^0 concentration, respectively. Besides, to reduce the experimental error, E_{NO} and E_{Hg} were the average of two or three parallel experimental data and the relative error was less than 5%.

3. Results and discussion

3.1. Samples characterization

3.1.1. BET analysis

The physical properties containing BET surface area, average pore diameter and total pore volume of virgin BAC and $Co_{0.4}Ce_{0.6}$/BAC are listed in Table 1. Moreover, the N_2 adsorption-desorption isotherms of these samples are displayed in Fig. 1a, all isotherms show the typical IV curve with hysteresis loops tape H3, indicating the presence of slit-like pores according to IUPAC [15]. Taken as a whole, virgin BAC owned the biggest BET surface area of 1029.22 m^2/g and the highest total pore volume of 0.690 cm^3/g. However, both BET surface area and total pore volume of $Co_{0.4}Ce_{0.6}$/BAC samples distinctly dropped with the increase of the loading value of metal oxides. This might be because that metal oxides dispersed on the external or internal surface of BACs, and excessive metal oxides loading would result in agglomeration and blocking some pores of BACs, thus decreasing total pore volume and BET surface area [11,30]. In addition, the pore size distribution curves of the samples were shown in Fig. 1b, taking the total pore volume into consideration, the pore volume characteristics were primarily determined by mesopore, macropore and micropore acted as auxiliary.

Table 1
The BET specific surface area and pore parameters of the samples.

Sample	BET surface area (m^2/g)	Total pore volume (cm^3/g)	Average pore diameter (nm)
Virgin BAC	1029.22	0.690	2.682
5%$Co_{0.4}Ce_{0.6}$/BAC	708.89	0.475	2.681
15%$Co_{0.4}Ce_{0.6}$/BAC	628.85	0.391	2.486
25%$Co_{0.4}Ce_{0.6}$/BAC	543.51	0.342	2.513

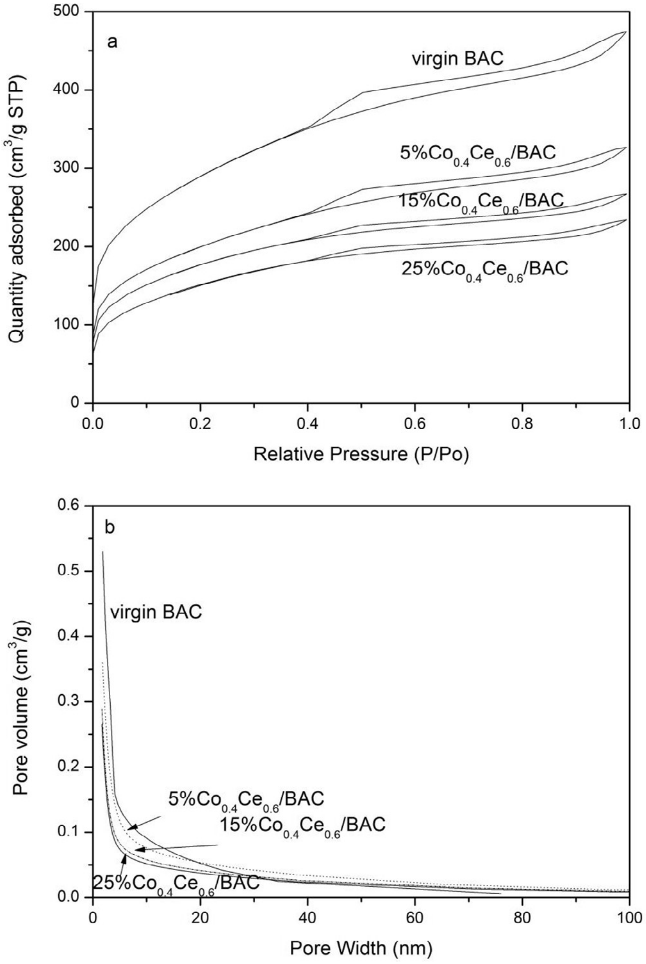

Fig. 1. The N_2 adsorption-desorption isotherms and pore size distribution curves of virgin BAC and $Co_{0.4}Ce_{0.6}$/BAC samples: (a) the N_2 adsorption-desorption isotherms, (b) the pore size distribution curves.

3.1.2. SEM analysis

The SEM images of virgin BAC and $Co_{0.4}Ce_{0.6}$/BAC with different loading value are shown in Fig. 2. The dark zones represented carbon enriched areas, whereas light zones indicated the presence of metal oxides. The surface characteristics of virgin BAC was changed by loading metal oxides, which mainly dispersed on the surface of BACs. It

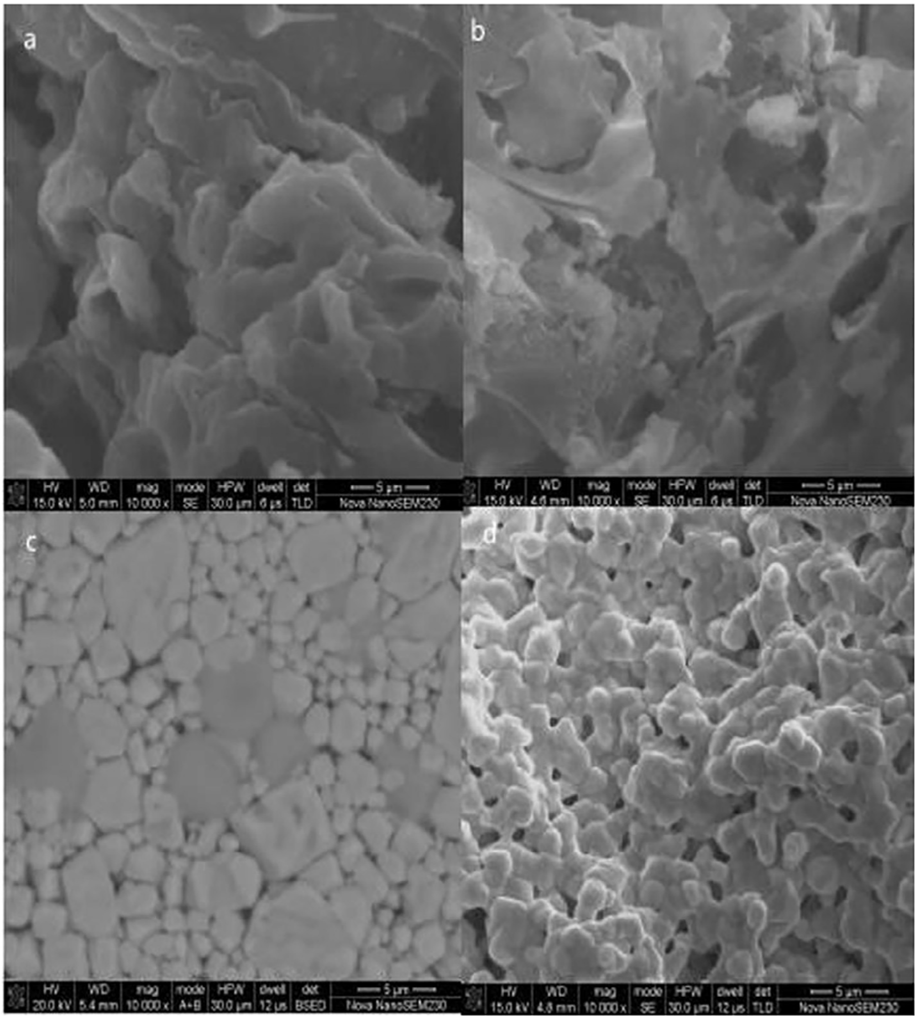

Fig. 2. SEM images of virgin BAC and 15%$Co_{0.4}Ce_{0.6}$/BAC: (a) Virgin BAC, (b) 5%$Co_{0.4}Ce_{0.6}$/AC, (c) 15%$Co_{0.4}Ce_{0.6}$/AC, (d) 25%$Co_{0.4}Ce_{0.6}$/AC. 10,000 multiplier.

could be clearly seen that 5%$Co_{0.4}Ce_{0.6}$/BAC had the best dispersion among these $Co_{0.4}Ce_{0.6}$/BAC samples and almost no agglomerate was observed, but it possessed the biggest dark zones, meaning that it couldn't provide abundant active centers for catalytic reactions. For 15%$Co_{0.4}Ce_{0.6}$/BAC, metal oxides highly scattered on the BAC surface, and only a few agglomerates were observed, while apparent agglomerates existed in 25%$Co_{0.4}Ce_{0.6}$/BAC. This was in accordance with the BET results. Combined XRD and SEM analyses, enough and high dispersion metal oxides on the surface of BACs were favorable for catalytic activities.

3.1.3. XRD analysis

Fig. 3 shows the XRD patterns of virgin BAC, 15%Co/BAC, 15%Ce/BAC and 15%Co_yCe_{1-y}/BAC. With regard to virgin BAC, two strong peaks at 26.60° and 44.46° (JCPDS 25-0284) were observed [6,29]. Nevertheless, the two peaks decreased or even disappeared with the introduction of cobalt oxide or cerium oxide, suggesting there was a strong interaction between these oxides and BAC. For 15%Co/BAC, five peaks at $2\theta = 26.60°$, 36.84°, 42.39°, 61.49° and 74.08° were detected, in which, except for the peak at 26.60° attributed to BAC, the peaks at 36.84° and 74.08° (JCPDS 09-0418) were ascribed to Co_3O_4 while the peaks at 42.39° and 61.49° (JCPDS 48-1719) belonged to CoO [14]. This indicated Co_3O_4 and CoO coexisted in the sample. Four peaks at $2\theta = 28.55°$, 33.08°, 47.49° and 56.33° (JCPDS 04-0593) were attributed to CeO_2 in 15%Ce/BAC [6,14]. Compared with 15%Ce/BAC and 15%Co/BAC, these peaks belonged to CeO_2 and CoO and Co_3O_4 weakened or even disappeared in 15%Co_yCe_{1-y}/BAC samples, respectively. This indicated cerium oxide crystallites and cobalt oxide crystallites in the 15%Co_yCe_{1-y}/BAC samples showed better dispersion compared with that of Co/BAC and Ce/BAC [31], besides, even amorphous surface species existed in these samples, which might be from the Co-Ce interaction and they were beneficial to catalytic reactions [14,20,31].

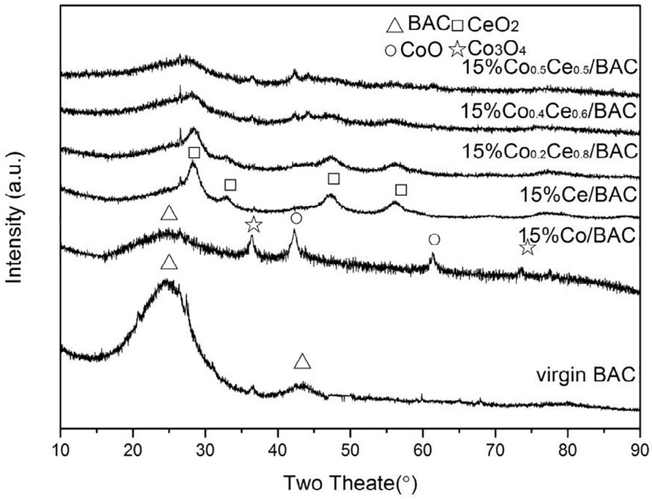

Fig. 3. XRD patterns of virgin BAC, 15%Co/BAC, 15%Ce/BAC and 15%Co_yCe_{1-y}/BAC.

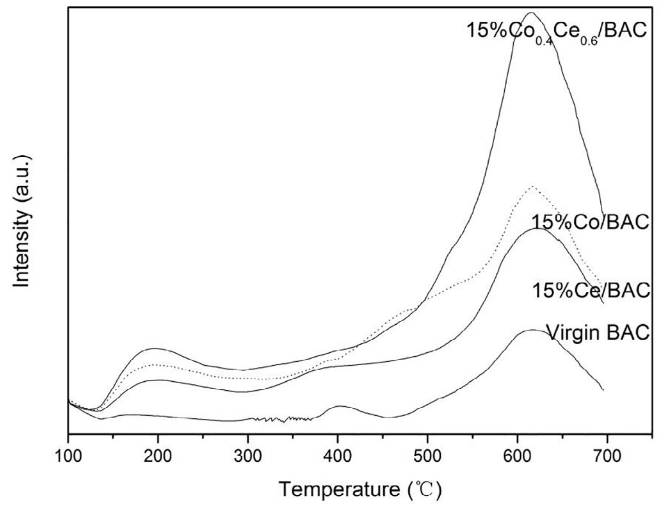

Fig. 4. NH_3-TPD curves of virgin BAC, 15%Co/BAC, 15%Ce/BAC and 15%$Co_{0.4}Ce_{0.6}$/BAC.

3.1.4. NH_3-TPD analysis

It is generally accepted that the surface acidity characteristics of catalysts play an important role for NH_3 adsorption and activation, which is of vital importance in the NH_3-SCR of NO reactions [6]. Therefore, NH_3-TPD was performed to estimate the surface acidic characteristic of virgin BAC, 15%Co/BAC, 15%Ce/BAC and 15%$Co_{0.4}Ce_{0.6}$/BAC. As shown in Fig. 4, it could be clearly seen that virgin BAC exhibited two narrowest and smallest desorption peaks, indicating it had the poorest acidity. After introducing Co or Ce species, two broader and bigger peaks were observed in supported BAC samples, suggesting that the total amount and strength of acid sites were significantly improved after loading metal oxides. Meanwhile, the total acid sites followed the ascending order: 15%Ce/BAC < 15%Co/BAC < 15%$Co_{0.4}Ce_{0.6}$/BAC. The weak desorption peaks at about 200 °C were assigned to Brønsted acid sites, whereas the strong peaks at around 625 °C were attributed to Lewis acid sites [32,33]. The Lewis acid sites were derived from unsaturated Co^{n+} or Ce^{n+} sites [32,34], while the Brønsted acid sites were associated with surface hydroxyl groups [32,35]. For 15%$Co_{0.4}Ce_{0.6}$/BAC, the most amount of Lewis acid sites might be due to the synergistic effect from Co and Ce species. Thus, the most acid sites of 15%$Co_{0.4}Ce_{0.6}$/BAC would cause a significant increase in adsorption capacity of NH_3, which was beneficial for the improvement of SCR activity.

3.1.5. H_2-TPR analysis

H_2-TPR measurements are applied to inspect the redox property of the samples and the results are illustrated in Fig. 5. 15%Ce/BAC exhibited one peak at around 570 °C, which would be assigned to the reduction of surface-capping oxygen species of CeO_2 [15,36]. Two reduction peaks centered about 318 °C and 420 °C were observed in the curve of 15%Co/BAC, the low temperature one was ascribed to the reduction step of Co^{3+} to Co^{2+}, whereas the high temperature one belonged to the reduction step of Co^{2+} to Co^0 [17,37]. The intensity of the low temperature peak was much smaller than that of the high temperature one, which indicated the quantity of Co^{2+} was bigger than that of Co^{3+} in the 15%Co/BAC [37]. Compared with 15%Ce/BAC and 15%Co/BAC, the reduction peaks of 15%$Co_{0.4}Ce_{0.6}$/BAC shifted to lower temperature, which demonstrated the reductive ability of surface active species in 15%$Co_{0.4}Ce_{0.6}$/BAC was enhanced. This also suggested the coexistence of ceria and cobalt oxides played a syngestic effect, resulting in significantly boosting reducibility of the samples with single active ingredient, which was beneficial to promoting NH_3-SCR of NO reactions [17,38,39]. Moreover, the quantities of Co^{3+} and Ce^{3+} were enhanced due to the coexistence of ceria and cobalt oxides as the Co 2p XPS analysis, which were correlated with catalytic activity, thus boosting the performance of the sample [27,28,37].

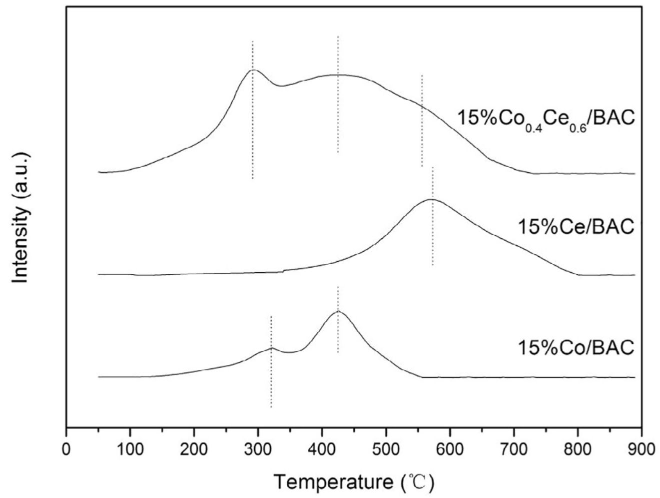

Fig. 5. H_2-TPR curves of 15%Co/BAC, 15%Ce/BAC and 15%$Co_{0.4}Ce_{0.6}$/BAC.

3.1.6. XPS analysis

XPS analysis was performed to evaluate the chemical states and composition of surface elements of virgin BAC, fresh and used 15%$Co_{0.4}Ce_{0.6}$/BAC. Fig. 6 displayed the spectra of O1s, Ce 3d, Co 2p and Hg 4f. The spectra of O 1s were presented in Fig. 6a. As for virgin BAC, two type peaks of O 1s were observed, the peak at 531.61 eV could be attributed to chemisorbed oxygen and/or weakly bonded oxygen, and the other peak at 533.46 eV was ascribed to either-type oxygen [21,40]. Both three type peaks of O 1s were observed on fresh and used 15%$Co_{0.4}Ce_{0.6}$/BAC samples, the peaks at 529.97 eV were regarded as lattice oxygen (denoted as O_α), the peaks at 531.57–531.78 eV were assigned to chemisorbed oxygen and/or weakly bonded oxygen (denoted as O_β), and the peaks at 532.83–532.87 eV represented hydroxyl groups or/and adsorbed water species (denoted as O_γ) [14,41,42]. It was noteworthy that the introduction of metal oxides resulted in the generation of O_α and the vanishing of either-type oxygen. The former could be attributed to metal oxides supplying both O_α and O_β, which possessed good mobility and oxygen vacancies [14,43,44]. Combing the analyses of BET and SEM, the loading and calcination processes of metal oxides could cover the surface of virgin BAC, thus blocking the either-type oxygen, which might be responsible for the later. Compared with fresh 15%$Co_{0.4}Ce_{0.6}$/BAC, the ratio of O_α decreased from 51.60% to 43.94% after the reaction while the ratios of O_β and O_γ demonstrated an upward tendency after the reaction, indicating O_α participated in the reactions. The increase of binding energy of O 1s after the reaction also proved that the ratio of O_α to other oxygen species dropped [45]. Compared to O_α and O_γ, O_β was more reactive in redox and oxidation reactions due to its greater mobility [42,43,46]. Moreover, our previous works indicated both O_α and O_β participated in the Hg^0 oxidation processes [6,14,44]. Therefore, it was reasonable to infer that more active oxygen would benefit for the NO reduction and Hg^0 oxidation processes [28,42].

The Ce 3d XPS spectra of fresh and used 15%$Co_{0.4}Ce_{0.6}$/BAC were presented in Fig. 6b, the peaks labeled as u, u_1, u_2 and u_3 were ascribed to Ce 3d3/2 spin-orbit states, while those peaks marked as v, v_1, v_2 and v_3 were attributed to Ce 3d5/2 states. Meanwhile, u/v, u_2/v_2 and u_3/v_3 doublets corresponded to Ce^{4+}, and u_1/v_1 were assigned to Ce^{3+} [42,44]. For both samples, Ce^{4+} and Ce^{3+} coexisted and Ce^{4+} was obviously predominant. The existence of Ce^{3+} might induce unsaturated chemical bonds and a charge imbalance, generating more chemisorbed oxygen and oxygen vacancies [47]. In addition, it had positive effects on the adsorption capacity of NH_3 and NO and the

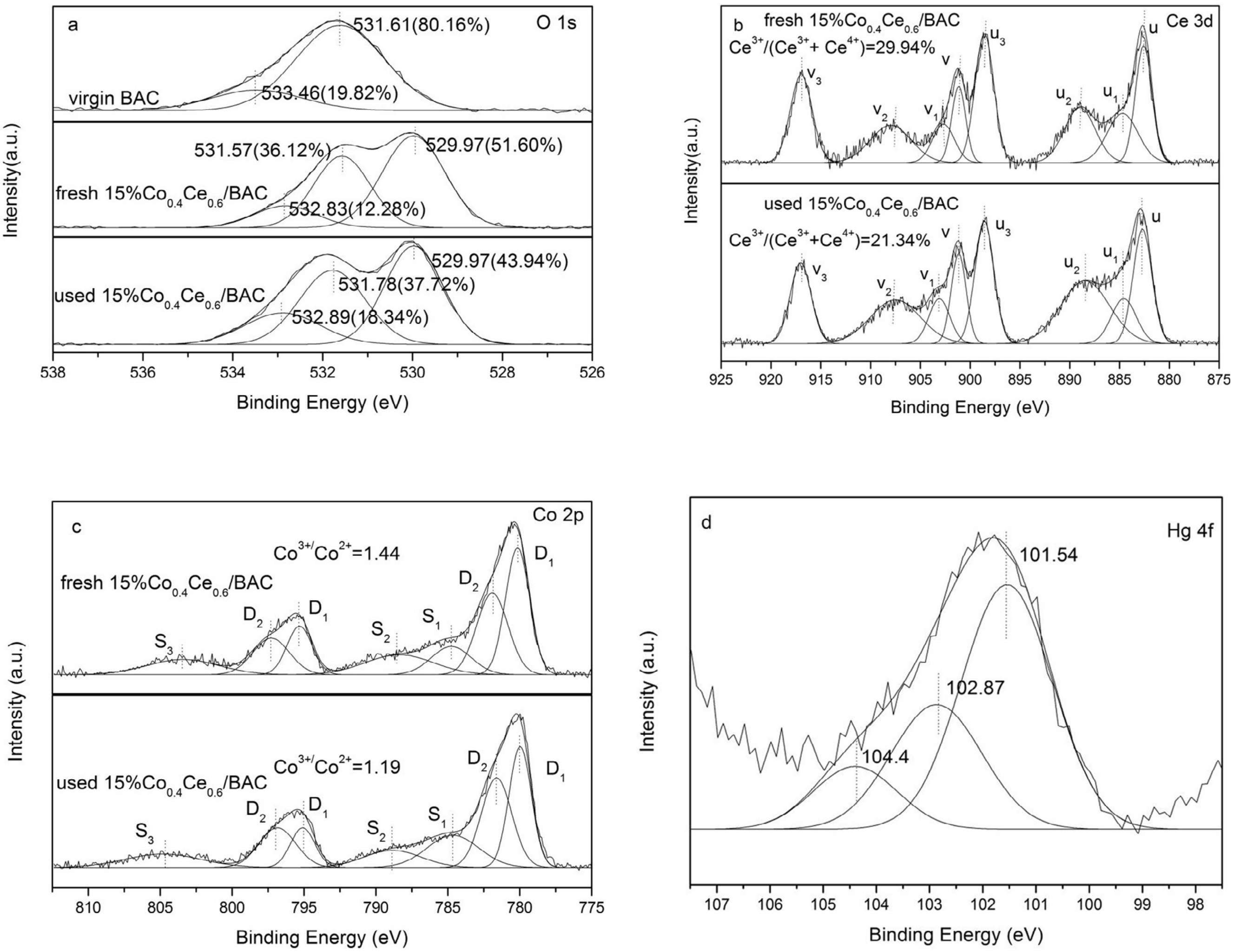

Fig. 6. XPS spectra of virgin BAC, fresh and used 15%$Co_{0.4}Ce_{0.6}$/BAC: (a) O 1s, (b) Ce 3d, (c) Co 2p and (d) Hg 4f.

sample' redox capability [48]. These were beneficial for NO reduction and Hg^0 oxidation processes, which were confirmed in our previous works [6,27,28]. After reactions, the ratio of Ce^{3+} decreased from 29.94% to 21.34% compared with the fresh sample, suggesting a redox reaction took place between Ce^{3+} and Ce^{4+}. The u_2 peak of used sample showed obviously broader compared with the fresh one, resulting in the increase of the value of u_2/v_2, which also indicated that Ce^{3+} participated in the reaction, generating more Ce^{4+}. The decrease of the Ce^{3+} ratio suggested that the transformation between Ce^{3+} and Ce^{4+} was not entirely balanced, a portion of Ce^{3+} irreversibly transformed to Ce^{4+} during the catalytic reactions [49]. Ce species shifted constantly between Ce^{3+} and Ce^{4+} with storing and releasing oxygen, meanwhile, the consumed Ce^{3+} was due to O_2 oxidizing Ce^{3+} to Ce^{4+} (Eq. (4)) and thus compensated the lattice oxygen rapidly (Eq. (5)).

$$Ce_2O_3 + 1/2O_2 \rightarrow 2CeO_2 \tag{4}$$

$$2CeO_2 \rightarrow Ce_2O_3 + O_\alpha \tag{5}$$

Fig. 6c presented the Co 2p XPS spectra of fresh and used 15%$Co_{0.4}Ce_{0.6}$/BAC, and they were deconvoluted into two spin-orbit doublets labeled as D_1 and D_2, and three satellite peaks denoted as S_1, S_2 and S_3. Meanwhile, D_1 at 780.2 eV ± 0.3 eV and a spin-orbital splitting of 15.1 eV were assigned to the octahedral Co^{3+} species. D_2 at 781.8 eV ± 0.2 eV and a spin-orbital splitting of 15.5 eV were attributed to the tetrahedral Co^{2+} species [19,50]. S_1 and S_2 satellite peaks corresponded to octahedral sites while S_3 satellite peak was attributed to tetrahedral sites [51]. These satellite peaks were an evidence of the presence Co species reduction from Co^{3+} to Co^{2+} in octahedral sites [19,52]. The Co^{3+}/Co^{2+} ratio of 1.44 in fresh 15%$Co_{0.4}Ce_{0.6}$/BAC was a little higher than that in the used sample (1.19), suggesting a reduction shift occurred as mentioned above. The decrease of the Co^{3+}/Co^{2+} ratio also indicated that the transformation between Co^{3+} and Co^{2+} was not entirely balanced, partial Co^{3+} was irreversibly transformed to Co^{2+} during the reactions.

The Hg4f XPS spectra of used 15%$Co_{0.4}Ce_{0.6}$/BAC were shown in Fig. 6d, three peaks at 101.54 eV, 102.87 eV and 104.4 eV were detected. The medium peak at 102.87 eV represented the Si 2p [29]. The strong peak at 101.54 eV was ascribed to Hg $4f_{7/2}$ and the weak peak at 104.4 eV was attributed to Hg $4f_{5/2}$, which were assigned to Hg 4f for HgO [27,29,53]. The presence of HgO was also confirmed by the mercury conversion test (Fig. 7). Although Fig. 7 indicated that both adsorption and oxidation contributed to E_{Hg}, no characteristic peak at 99.9 eV for adsorbed Hg^0 was observed [29,53]. The reason was that the result of XPS was the experiment proceeding for 80 h when the adsorbed Hg^0 was negligible and oxidizing Hg^0 to HgO mainly contributed to E_{Hg}.

3.1.7. FTIR analysis

FTIR spectra about adsorbing different gaseous components were performed in Fig. 8. As a whole, all the samples shared some similar bands that might be mainly due to the nature of the carrier. For instance, the obvious band at 1290 cm^{-1} was attributed to asymmetric stretching vibrations of C—O—C in ester groups [21]. Several new bands

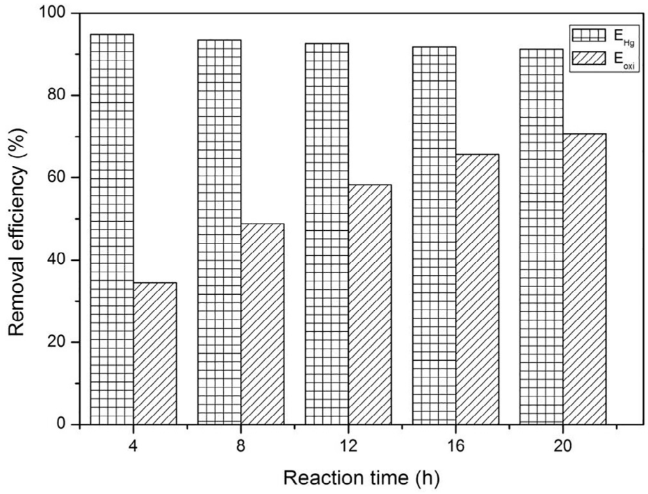

Fig. 7. The results of mercury conversion tests. Reaction conditions: T = 230 °C, 6% O_2, 100ug/m^3 Hg^0, 600 ppm NO, 600 ppm NH_3, N_2 as balance.

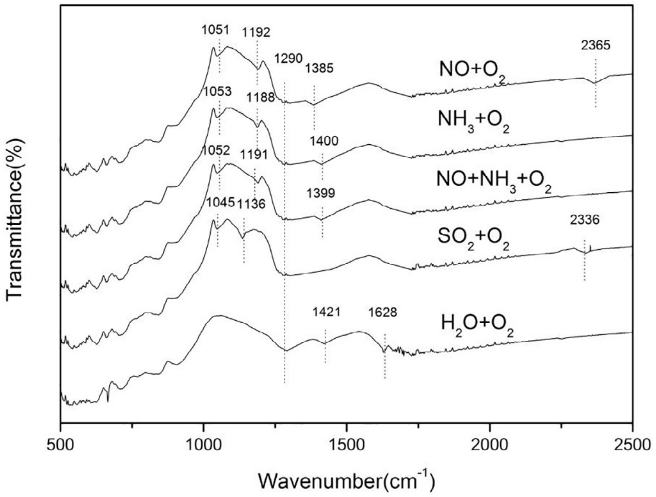

Fig. 8. FTIR spectra for 15%$Co_{0.4}Ce_{0.6}$/BAC. Reaction conditions: NO + O_2 (600 ppm NO + 6% O_2), NH_3 + O_2 (600 ppm NH_3 + 6% O_2), NO + NH_3 + O_2 (600 ppm NO + 600 ppm NH_3 + 6% O_2), SO_2 + O_2 (300 ppm SO_2 + 6% O_2), H_2O + O_2 (5 vol.% H_2O + 6% O_2) and N_2 as balance gas.

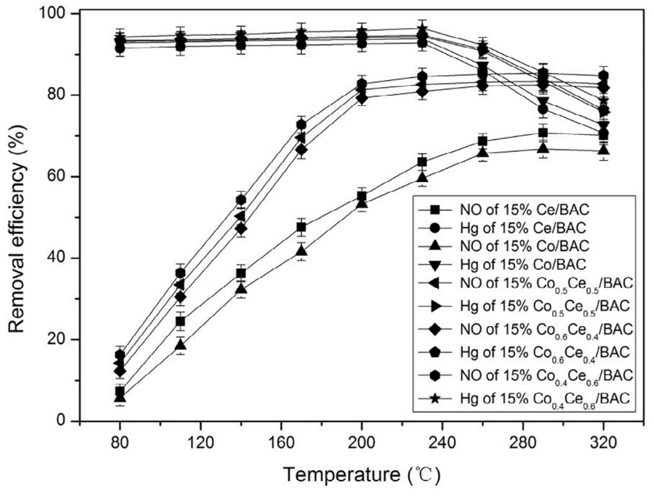

Fig. 9. Effect of active ingredient on simultaneous NO and Hg^0 removal. Reaction conditions: T = 80–320 °C, 6% O_2, 100 μg/m^3 Hg^0, 600 ppm NO, 600 ppm NH_3, N_2 as balance.

at 1051, 1192, 1385, 2365 cm^{-1} were observed after adsorbing NO + O_2. The band at 1051 cm^{-1} could be attributed to nitrato and nitrito species [54]. The band at 1192 cm^{-1} was ascribed to anionic nitrosyl NO– that could transfer to nitrite or nitrate [27]. The band at 1385 cm^{-1} corresponded to nitrate species and the band at 2365 cm^{-1} was ascribed to overtone vibrations of nitrato species [28,55]. Three new bands at 1053, 1188, 1400 cm^{-1} were detected in the NH_3 + O_2 adsorption spectra. The bands at 1053 and 1188 cm^{-1} were ascribed to coordinated NH_3 bound to Lewis acid sites while the weak band at 1400 cm^{-1} was assigned to ammonium ion on Brønsted acid sites [27,55,56]. This indicated NH_3 could be simultaneously adsorbed on Lewis acid sites and Brønsted acid sites, suggesting both acid sites might contribute to the denitration reactions. In the spectra of NO + NH_3 + O_2 adsorption, the sharp band at about 1052 cm^{-1} might be the overlapping of nitrato and nitrito and coordinated NH_3 bound to Lewis acid sites [27,55]. Similarly, the obvious band at 1191 cm^{-1} could be also considered as the overlapping of anionic nitrosyl NO– and coordinated NH_3 on Lewis acid sites [27,55]. The band at 1399 cm^{-1} corresponded to ammonium bound to Brønsted acid sites [55,56]. This demonstrated that NO and NH_3 could be adsorbed simultaneously on corresponding adsorption sites, which might be transferred into some intermediates participating in the denitration reactions.

When the sample treated by SO_2 + O_2, some characteristic bands were detected. The band centered at 1045 cm^{-1} was proposed to be the stretching vibrations of adsorbed sulfates or bisulfates [57], which could heighten the acidity of the sample and promote the adsorption of NH_3 and its intermediates, thus partly alleviating the inhibition effect of SO_2 [11]. In addition, the band observed at 1136 cm^{-1} was assigned to gas-phase SO_2 and the band at 2336 cm^{-1} was demonstrated as liquidlike physisorbed SO_2 [57,58]. As a result, the presence of adsorbed SO_2 could restrict the removal of NO and Hg^0 to some degree due to the competition effect, as shown in Fig. 10. After adsorbing H_2O + O_2, the characteristic band appeared at 1628 cm^{-1} could be ascribed to dHOH of H_2O [2]. Besides, the band observed at 1421 cm^{-1} corresponded to the presence of water [27]. The presence of H_2O could negatively affect the removal of NO and Hg^0 due to the competition effect, which was in accordance with the results of Fig. 11.

3.2. The performance of samples

3.2.1. Effect of active ingredient

Fig. 9 displayed the performances of 15%Ce/BAC, 15%Co/BAC and 15%Co_yCe_{1-y}/BAC samples on simultaneous removal of NO and Hg^0 at

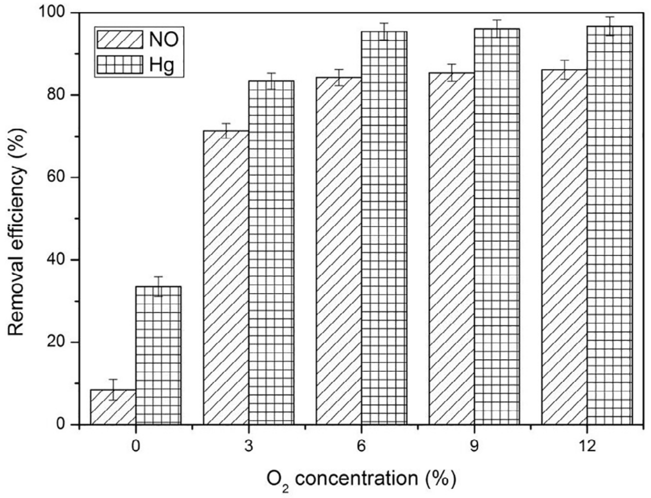

Fig. 10. Effect of the concentration of O_2 on simultaneous NO and Hg^0 removal over 15%$Co_{0.4}Ce_{0.6}$/BAC. Reaction conditions: T = 230 °C, 0–12% O_2, 100 μg/m^3 Hg^0, 600 ppm NO, 600 ppm NH_3, N_2 as balance.

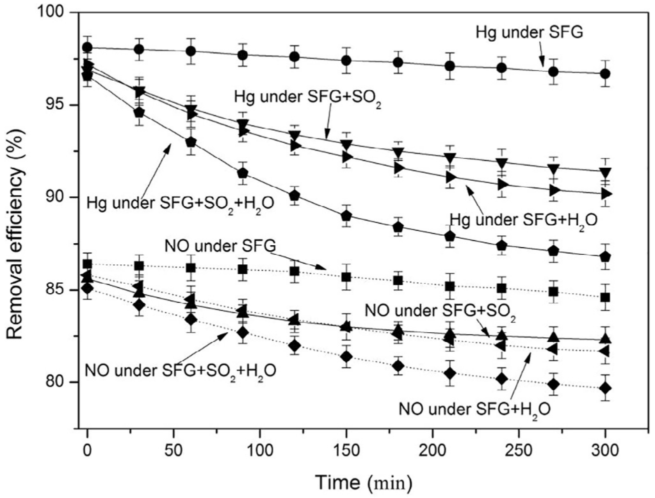

Fig. 11. The separate or synchronous effects of SO_2 and H_2O on simultaneous NO and Hg^0 removal over 15%$Co_{0.4}Ce_{0.6}$/BAC. Reaction conditions: T = 230 °C, 6% O_2, 100 ug/m^3 Hg^0, 600 ppm NO, 600 ppm NH_3, 400 ppm SO_2(when used), 5vol.%H_2O(when used), N_2 as balance.

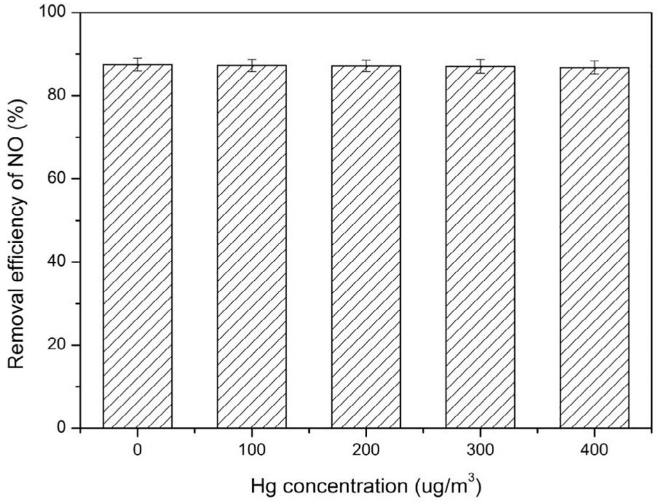

Fig. 12. Effect of the concentration of Hg^0 on NO removal over 15%$Co_{0.4}Ce_{0.6}$/BAC. Reaction conditions: T = 230 °C, 6% O_2, 0–400 μg/m^3 Hg^0, 600 ppm NO, 600 ppm NH_3, N_2 as balance.

80–320 °C. E_{NO} and E_{Hg} over these samples almost shared the similar trend. Thereinto, E_{NO} exhibited an obvious increase with the increase of reaction temperature from 80 °C to 260 °C and afterwards showed different trends, while E_{Hg} yielded a very slight raise in the temperature range of 80–230 °C and then decreased distinctly with further increasing reaction temperature. The obvious decrease of E_{Hg} at high temperature could be explained by two possible reasons. One was attributed to high temperature inhibiting Hg^0 adsorption [28,43]. In addition, high temperature did some damage to the carrier' structure of BAC because a very little amounts of CO and CO_2 were detected in the outlet gas at 290 °C and 320 °C, which was discussed in more detail in the part of mechanism study. Compared with 15%Ce/BAC and 15%Co/BAC, 15%Co_yCe_{1-y}/BAC shown better E_{NO} and E_{Hg}, indicating that a synergistic effect took place between CoO_x and CeO_2 when they coexisted. This synergistic effect was also observed in other reports [6,14,44]. Among these 15%Co_yCe_{1-y}/BAC samples, 15%$Co_{0.4}Ce_{0.6}$/BAC manifested the best performance and it possessed E_{NO} of 84.7% and E_{Hg} of 96.8% at 230 °C.

3.2.2. Effect of O_2

The effects of O_2 on simultaneous removal of NO and Hg^0 over 15%$Co_{0.4}Ce_{0.6}$/BAC were shown in Fig. 10. The sample exhibited poor performance for NO and Hg^0 removal in the absence of O_2, which was due to adsorption and weak reactions from the chemisorbed oxygen and lattice oxygen existed on the surface of 15%$Co_{0.4}Ce_{0.6}$/BAC, as shown in the O 1s XPS analysis. Higher E_{NO} and E_{Hg} were achieved after the addition of 3% O_2 and they obtained further obvious increase when the concentration of O_2 increased from 3% to 6%. A continued raise of the concentration of O_2 to 9% or even to 12% engendered little impact on Hg^0 and NO removal. This indicated O_2 could markedly promote Hg^0 and NO removal under insufficient oxygen conditions and gaseous O_2 could replenish the consumed lattice and chemisorbed oxygen [28,59], which were consistent with other reports [60,61].

3.2.3. Effects of SO_2 and H_2O

The separate or synchronous effects of SO_2 and H_2O on NO and Hg^0 simultaneous removal over 15%$Co_{0.4}Ce_{0.6}$/BAC were illustrated in Fig. 11. It was detected that SO_2 and H_2O had inhibitory influence on both NO and Hg^0 removal, and the negative effect increased with the increase of the concentrations of SO_2 and H_2O in our previous works [6,27,44]. Combined with the FTIR analysis and literatures, the adverse effect of SO_2 could be explained by two reasons, on one hand, the competitive effect existed among SO_2 and NO, NH_3 and Hg^0 for adsorption or catalytic sites [27,62]. On the other hand, the possible formation of ammonium sulfates or other sulfates would destroy the sample's porous structure and block the activated centers [28,63], thus leading to the decrease of E_{NO} and E_{Hg}. Similarly, the competitive adsorption among H_2O, Hg^0, NH_3 and NO was responsible for the decrease of E_{Hg} and E_{NO} by H_2O [28,43,64].

Fig. 11 also revealed that the synchronous effect of 400 ppm SO_2 and 5% H_2O induced an obvious drop of E_{NO} and E_{Hg}, compared with that of the separate effects of SO_2 and H_2O. The obvious drop of E_{NO} and E_{Hg} was ascribed to the synergistic competition effects and the possible formation of ammonium sulfates (bisulfates) or other sulfates due to the coexistence of SO_2 and H_2O and other gas components. The more serious deactivation effect derived from the combined influence of SO_2 and H_2O was also found in our previous works [6,11].

3.3. The interaction between NO removal and Hg^0 removal

3.3.1. Effect of Hg^0 on NO removal

Hg^0 was a pivotal component in the SFG, which might have an influence on NO removal. Therefore, the effects of different concentrations of Hg^0 on NO removal over 15%$Co_{0.4}Ce_{0.6}$/BAC were illustrated in Fig. 12. For contrast, the test under Hg-free flue gas condition was performed. E_{NO} didn't display any palpable change after the introduction of 100 μg/m^3 Hg^0. However, E_{NO} demonstrated a slight decrease with further increase of the concentration of Hg^0, indicating that Hg^0 had mildly inhibitory effect on NO removal. Two possible reasons could be responsible for this prohibitive phenomenon. For one thing, it was easy to understand that Hg^0 could compete with NO and NH_3 for adsorption or catalytic sites. For another thing, the XPS analysis had confirmed that the formation of HgO accumulated on the surface of the sample due to the oxidation reaction of Hg^0, and the accumulated HgO might cover some activated centers, resulting in a slight drop of E_{NO} [28,42]. Fortunately, it was noteworthy that the concentration of Hg^0 in actual condition was much lower than that in the tested conditions and the presence of Hg^0 only had slight effect on NH_3-SCR of NO in the practical application.

3.3.2. Effects of SCR atmosphere on Hg^0 removal

As shown in Fig. 13, the effects of SCR atmosphere (NO and NH_3) on Hg^0 removal over 15%$Co_{0.4}Ce_{0.6}$/BAC were investigated. The blank test of Hg^0 removal was carried out when NO and NH_3 were removed from the SFG. The blank test yielded better E_{Hg} than that under SFG conditions, suggesting that the coexistence of 600 ppm NH_3 and 600 ppm NO

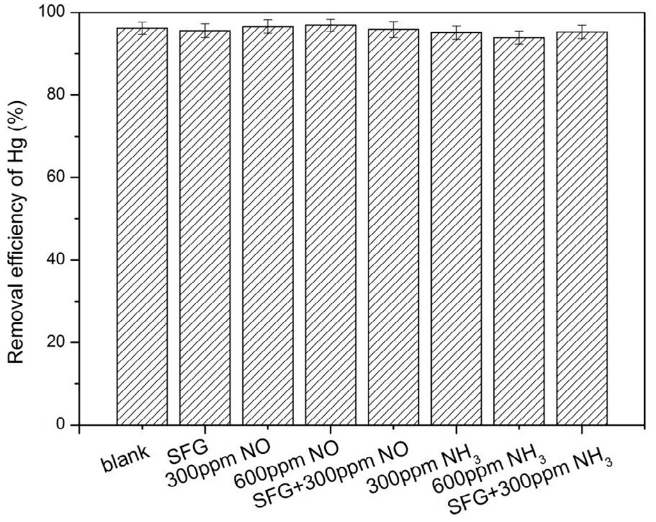

Fig. 13. Effect of SCR atmosphere (NH_3 and NO) on Hg^0 removal over 15%$Co_{0.4}Ce_{0.6}$/BAC. Reaction conditions: T = 230 °C, 6% O_2, 100 μg/m^3 Hg^0, 0–900 ppm NO, 0–900 ppm NH_3, N_2 as balance. SFG contained 100 μg/m^3 Hg^0, 6%O_2, 600 ppm NO, 600 ppm NH_3, N_2 as balance.

could negatively affect Hg^0 removal, which was in agreement with previous works [2,4,6,28]. It was conjectured that SCR reaction prevailed over the Hg^0 oxidation reaction when NO reduction and Hg^0 oxidation reactions coexisted under high concentrations of NH_3 and NO [28,65].

To further identify the several effect of NO and NH_3 on Hg^0 removal, a battery of tests with different various concentrations of NO or NH_3 were undergone. A slightly propulsive effect of NO alone on Hg^0 removal was observed and the promotional role boosted lightly with the increase of the concentration of NO. This phenomenon also appeared under the conditions that NH_3 and more NO coexisted in the flue gas. As mentioned in the FTIR analysis, NO could weakly absorb on the surface of the sample, and some of these absorbed NO might react with the surface oxygen to generate NO_2, which was reported to be active for Hg^0 oxidation [44,66]. On the contrary, the presence of NH_3 alone displayed some inhibitory effect on Hg^0 removal and this appearance was also detected under the conditions that NO and more NH_3 coexisted in the flue gas. The inhibitory effect of NH_3 on Hg removal might be explained by that NH_3 could rapidly adsorb on the sample surface and afterwards some adsorbed species generated, which might consume surface active oxygen and occupy the surface active sites to inhibit Hg^0 oxidation, thus resulting in a decrease of E_{Hg} [55,67].

3.4. Mechanism study

According to the results of characterizations and previous works, it was proposed that the synergistic effect emerged between ceria and cobalt oxide, meanwhile, some CeO_2 was transformed to Ce_2O_3 while part Co^{2+} was shifted to Co^{3+}, producing some Co_3O_4 (Eq. (6)) [14]. It was deemed that ample Co^{3+} possibly increased anionic defects resulting from special porous channels and larger surface areas and the quantity of Co^{3+} on the sample surface was correlated with catalytic activity [37]. In addition, Ce^{3+} could induce unsaturated chemical bonds and a charge imbalance, generating more chemisorbed oxygen and oxygen vacancies [47]. Moreover, the redox shift between Ce^{3+} and Ce^{4+} could be conducive to simultaneous NO and Hg^0 removal. As a result, the synergistic effect between ceria and cobalt oxide was beneficial for NO reduction and Hg^0 oxidation reactions.

Fig. 7 indicated both adsorption and Hg^0 oxidation contributed to Hg^0 removal, whose contributions varied with reaction time and Hg^0 oxidation prevailed gradually. It was speculated that both O_α and O_β took place the Hg^0 oxidation reactions (Eqs. (11) and (12)) [27,28,44]. However, O_α might play the predominant role in this work (Eq. (11)), as shown in the XPS O 1s analysis, which was in accordance with our previous work [14]. Gas-phase oxygen could replenish the consumed O_α and O_β and reoxidize the reduced metal oxides (Eqs. (4), (8) and (9)) [68]. Combined with the characterization analyses and the literatures, it was surmised that the Hg^0 oxidation reaction over 15%$Co_{0.4}Ce_{0.6}$/BAC mainly followed the Mars-Masson mechanism [14,69,70]. It was speculated that Hg^0(g) was preferentially adsorbed on the surface of the sample to form adsorbed Hg^0(ad) and afterwards it would be oxidized into HgO(ad) by O_α and O_β, meanwhile, part of HgO(ad) might convert into HgO(g). The reaction pathways could be summarized as follows:

$$2CeO_2 + 3CoO \rightarrow Ce_2O_3 + Co_3O_4 \tag{6}$$

$$Co_3O_4 \rightarrow 3CoO + O_\alpha \tag{7}$$

$$3CoO + 1/2\ O_2 \rightarrow Co_3O_4 \tag{8}$$

$$O_2 + \text{surface–BAC} \rightarrow 2O_\beta \tag{9}$$

$$Hg^0(g) + \text{surface–BAC} \rightarrow Hg^0(ad) \tag{10}$$

$$Hg^0(ad) + O_\alpha \rightarrow HgO(ad) \tag{11}$$

$$Hg^0(ad) + O_\beta \rightarrow HgO(ad) \tag{12}$$

$$HgO(ad) \rightarrow HgO(g) \tag{13}$$

For NH_3-SCR of NO, it was well accepted that catalytic centers of metal oxides loaded catalysts were active metal oxides, which were considered as electron transfer stations among NH_3, NO and O_2 [6,13,16,71,72]. On the basis of these literatures and the results of characterizations and tests, Co-Ce metal oxides (denoted as MO) acted as catalytic centers in this work. Therefore, chief reaction pathways were inferred as follows: NH_3 was firstly coordinated to Brønsted sites or Lewis acid sites while some NO was oxidized to NO_2 absorbed on the surface of the sample, then adsorbed NH_3 species reacted with gaseous NO and adsorbed NO_2, thus forming the final products of N_2 and H_2O. These reactions were summarized as Eq. (9) and Eqs. ((14)–(19)), which was mainly ascribed to the Langmuir-Hinshlwood mechanism [13,27]. Notably, very little amounts of CO and CO_2 were detected at 290 °C and 320 °C in the outlet gases, indicating some side reactions occurred along with NO reduction and Hg^0 oxidation processes due to the carrier of carbon as a reducing agent, as shown in Eqs. ((20)–(22)), thus destroying the carrier structure to some degree and resulting in the decrease of E_{Hg} and even E_{NO}. This phenomenon was also observed in other NO reduction reactions over carbon carrier loaded metal oxides [6,16,73]. Notwithstanding, these side reactions were much weaker compared with NO reduction and Hg^0 oxidation reactions at low temperatures (< 260 °C).

$$MO + O_\beta \leftrightarrow MO_2^* \tag{14}$$

$$MO_2^* + NO(g) \leftrightarrow MO + NO_2(ad) \tag{15}$$

$$NH_3(g) \rightarrow NH_3(ad) \tag{16}$$

$$NH_3(g) + H^+ \rightarrow NH_4^+(ad) \tag{17}$$

$$2NH_3(ad) + 2NO_2(ad) + NO(g) \rightarrow 2N_2 + 3H_2O \tag{18}$$

$$2NH_4^+(ad) + NO_2(ad) + NO(g) \rightarrow 2N_2 + 3H_2\ O + 2H^+ \tag{19}$$

$$MO_2^* + \text{surface–BAC} \rightarrow MO + CO \tag{20}$$

$$MO_2^* + CO \rightarrow MO + CO_2 \tag{21}$$

$$2NO + 2CO + O_2 \rightarrow N_2 + 2CO_2 \tag{22}$$

4. Conclusion

A series of CoO_x-CeO_2 loaded maize straw derived biomass activated carbon (CoCe/BAC) samples were applied for simultaneous NO and Hg^0 removal. 15%$Co_{0.4}Ce_{0.6}$/BAC yielded prominent Hg^0 removal efficiency (96.8%) and superior NO removal efficiency (84.7%) at 230 °C. The separate or synchronous deactivation effects of 400 ppm SO_2 and 5% H_2O were detected. The interaction between NO removal and Hg^0 removal was investigated, the results demonstrated that the presence of abundant Hg^0 exhibited very slightly inhibitory effect on NO removal, and NH_3 negatively affected Hg^0 removal, whereas NO mildly boosted Hg^0 removal in presence of O_2. The characterization analyses indicated the excellent performance of 15%$Co_{0.4}Ce_{0.6}$/BAC could be ascribed to its better texture properties, lower crystallinity and stronger redox ability. Besides, a synergetic effect appeared between cobalt oxide and cerium oxide, resulting in generating more Ce^{3+} and Co^{3+} to induce more anionic defects and produce more active oxygen and oxygen vacancies. The mechanisms of simultaneous removal of NO and Hg^0 were probed and proposed based on the characterizations and literatures. NO reduction reactions were mainly assigned to the Langmuir-Hinshlwood mechanism while both adsorption and Hg^0 oxidation contributed to Hg^0 removal. Meanwhile, Hg^0 oxidation corresponded to the Mars-Masson mechanism prevailed gradually with the increase of reaction time.

Acknowledgements

This work was financially supported by the National Natural Science Foundation of China – China (51478173), the National Key Research and Development Program of China – China (2016YFC0204104) and the Scientific and Technological Major Special Project of Hunan Province in China – China (2015SK1003).

References

[1] L. Fan, L. Ling, B. Wang, R. Zhang, The adsorption of mercury species and catalytic oxidation of Hg^0 on the metal-loaded activated carbon, Appl. Catal. A: Gen. 520 (2016) 13–23.

[2] L. Zhao, C. Li, S. Li, Y. Wang, J. Zhang, T. Wang, G. Zeng, Simultaneous removal of elemental mercury and NO in simulated flue gas over V_2O_5/ZrO_2-CeO_2 catalyst, Appl. Catal. B: Environ. 198 (2016) 420–430.

[3] M. Hui, Q. Wu, S. Wang, S. Liang, L. Zhang, F. Wang, M. Lenzen, Y. Wang, L. Xu, Z. Lin, H. Yang, Y. Lin, T. Larssen, M. Xu, J. Hao, Mercury flows in China and global drivers, Environ. Sci. Technol. 51 (2017) 222–231.

[4] H. Li, S. Wu, C.Y. Wu, J. Wang, L. Li, K. Shih, SCR atmosphere induced reduction of oxidized mercury over CuO-CeO_2/TiO_2 catalyst, Environ. Sci. Technol. 49 (2015) 7373–7379.

[5] H. Xu, Z. Qu, C. Zong, W. Huang, F. Quan, N. Yan, MnOx/Graphene for the catalytic oxidation and adsorption of elemental mercury, Environ. Sci. Technol. 49 (2015) 6823–6830.

[6] L. Gao, C. Li, P. Lu, J. Zhang, X. Du, S. Li, L. Tang, J. Chen, G. Zeng, Simultaneous removal of Hg^0 and NO from simulated flue gas over columnar activated coke granules loaded with La_2O_3-CeO_2 at low temperature, Fuel 215 (2018) 30–39.

[7] S. Sjostrom, M. Durham, C.J. Bustard, C. Martin, Activated carbon injection for mercury control: overview, Fuel 89 (2010) 1320–1322.

[8] Y. Yang, J. Liu, B. Zhang, F. Liu, Mechanistic studies of mercury adsorption and oxidation by oxygen over spinel-type $MnFe_2O_4$, J. Hazard. Mater. 321 (2017) 154–161.

[9] E. Sasmaz, A. Kirchofer, A.D. Jew, A. Saha, D. Abram, T.F. Jaramillo, J. Wilcox, Mercury chemistry on brominated activated carbon, Fuel 99 (2012) 188–196.

[10] Y. Zhao, R. Hao, M. Qi, Integrative process of preoxidation and absorption for simultaneous removal of SO_2, NO and Hg^0, Chem. Eng. J. 269 (2015) 159–167.

[11] L. Qu, C. Li, G. Zeng, M. Zhang, M. Fu, J. Ma, F. Zhan, D. Luo, Support modification for improving the performance of MnO_x–CeO_y/γ-Al_2O_3 in selective catalytic reduction of NO by NH_3, Chem. Eng. J. 242 (2014) 76–85.

[12] H.S. Gandhi, G.W. Graham, R.W. McCabe, Automotive exhaust catalysis, J. Catal. 216 (2003) 433–442.

[13] J. Wang, Z. Yan, L. Liu, Y. Zhang, Z. Zhang, X. Wang, Low-temperature SCR of NO with NH_3 over activated semi-coke composite-supported rare earth oxides, Appl. Surf. Sci. 309 (2014) 1–10.

[14] H. Wu, C. Li, L. Zhao, J. Zhang, G. Zeng, Y. Xie, X. Zhang, Y. Wang, Removal of gaseous elemental mercury by cylindrical activated coke loaded with Co_Ox-Ce_O2 from simulated coal combustion flue gas, Energy Fuels 29 (2015) 6747–6757.

[15] H. Chen, Y. Xia, H. Huang, Y. Gan, X. Tao, C. Liang, J. Luo, R. Fang, J. Zhang, W. Zhang, X. Liu, Highly dispersed surface active species of Mn/Ce/TiW catalysts for high performance at low temperature NH_3-SCR, Chem. Eng. J. 330 (2017) 1195–1202.

[16] P. Lu, C. Li, G. Zeng, L. He, D. Peng, H.C. Li, Y. Zhai, Low temperature selective catalytic reduction of NO by activated carbon fiber loading lanthanum oxide and ceria, Appl. Catal. B: Environ. 96 (2010) 157–161.

[17] L. Zhang, L. Shi, L. Huang, J. Zhang, R. Gao, D. Zhang, Rational design of high-performance DeNOx catalysts based on $Mn_xCo_{3-x}O_4$ nanocages derived from metal–organic frameworks, ACS Catal. 4 (2014) 1753–1763.

[18] S. Lin, G. Su, M. Zheng, D. Ji, M. Jia, Y. Liu, Synthesis of flower-like Co_3O_4–CeO_2 composite oxide and its application to catalytic degradation of 1,2,4-trichlorobenzene, Appl. Catal. B: Environ. 123–124 (2012) 440–447.

[19] C. Wang, C. Zhang, W. Hua, Y. Guo, G. Lu, Sonia Gil, A. Giroir-Fendler, Catalytic oxidation of vinyl chloride emissions over Co-Ce composite oxide catalysts, Chem. Eng. J. 315 (2017) 392–402.

[20] J. Li, G. Lu, G. Wu, D. Mao, Y. Wang, Y. Guo, Promotional role of ceria on cobaltosic oxide catalyst for low-temperature CO oxidation, Catal. Sci. Technol. 2 (2012) 1865–1871.

[21] J. Ma, C. Li, L. Zhao, J. Zhang, J. Song, G. Zeng, X. Zhang, Y. Xie, Study on removal of elemental mercury from simulated flue gas over activated coke treated by acid, Appl. Surf. Sci. 329 (2015) 292–300.

[22] H. Zhang, J. Hu, Y. Qi, C. Li, J. Chen, X. Wang, J. He, S. Wang, J. Hao, L. Zhang, L. Zhang, Y. Zhang, R. Li, S. Wang, F. Chai, Emission characterization, environmental impact, and control measure of PM2.5 emitted from agricultural crop residue burning in China, J. Clean. Prod. 149 (2017) 629–635.

[23] M.N. Mahamad, M.A.A. Zaini, Z.A. Zakaria, Preparation and characterization of activated carbon from pineapple waste biomass for dye removal, Int. Biodeter. Biodegr. 102 (2015) 274–280.

[24] S. Singh, M.A. Nahil, X. Sun, C. Wu, J. Chen, B. Shen, P.T. Williams, Novel application of cotton stalk as a waste derived catalyst in the low temperature SCR-deNOx process, Fuel 105 (2013) 585–594.

[25] G. Li, S. Wang, Q. Wu, F. Wang, B. Shen, Mercury sorption study of halides modified bio-chars derived from cotton straw, Chem. Eng. J. 302 (2016) 305–313.

[26] J. Zeng, C. Li, L. Zhao, L. Gao, X. Du, J. Zhang, L. Tang, G. Zeng, Removal of elemental mercury from simulated flue gas over peanut shells carbon loaded with iodine ions, manganese oxides, and zirconium dioxide, Energy Fuels 31 (2017) 13909–13920.

[27] T. Wang, C. Li, L. Zhao, J. Zhang, S. Li, G. Zeng, The catalytic performance and characterization of ZrO_2 support modification on CuO-CeO_2/TiO_2 catalyst for the simultaneous removal of Hg^0 and NO, Appl. Surf. Sci. 400 (2017) 227–237.

[28] J. Zhang, C. Li, L. Zhao, T. Wang, S. Li, G. Zeng, A sol-gel Ti-Al-Ce-nanoparticle catalyst for simultaneous removal of NO and Hg^0 from simulated flue gas, Chem. Eng. J. 313 (2017) 1535–1547.

[29] S. Tao, C. Li, X. Fan, G. Zeng, P. Lu, X. Zhang, Q. Wen, W. Zhao, D. Luo, C. Fan, Activated coke impregnated with cerium chloride used for elemental mercury removal from simulated flue gas, Chem. Eng. J. 210 (2012) 547–556.

[30] J.C. Serrano-Ruiz, E.V. Ramos-Fernández, J. Silvestre-Albero, A. Sepúlveda-Escribano, F. Rodríguez-Reinoso, Preparation and characterization of CeO_2 highly dispersed on activated carbon, Mater. Res. Bull. 43 (2008) 1850–1857.

[31] H. Li, G. Lu, D. Qiao, Y. Wang, Y. Guo, Y. Guo, Catalytic methane combustion over Co_3O_4/CeO_2 composite oxides prepared by modified citrate sol–gel method, Catal. Lett. 141 (2011) 452–458.

[32] T. Gu, Y. Liu, X. Weng, H. Wang, Z. Wu, The enhanced performance of ceria with surface sulfation for selective catalytic reduction of NO by NH_3, Catal. Commun. 12 (2010) 310–313.

[33] D. Fang, F. He, X. Liu, K. Qi, J. Xie, F. Li, C. Yu, Low temperature NH_3-SCR of NO over an unexpected Mn-based catalyst: promotional effect of Mg doping, Appl. Surf. Sci. 427 (2018) 45–55.

[34] L. Zhu, Y. Zeng, S. Zhang, J. Deng, Q. Zhong, Effects of synthesis methods on catalytic activities of CoO_x–TiO_2 for low-temperature NH_3-SCR of NO, J. Environ. Sci.-China 54 (2017) 277–287.

[35] Z. Ma, X. Wu, Z. Si, D. Weng, J. Ma, T. Xu, Impacts of niobia loading on active sites and surface acidity in NbO_x/CeO_2–ZrO_2 NH_3–SCR catalysts, Appl. Catal. B: Environ. 179 (2015) 380–394.

[36] T. Boningari, P.R. Ettireddy, A. Somogyvari, Y. Liu, A. Vorontsov, C.A. McDonald, P.G. Smirniotis, Influence of elevated surface texture hydrated titania on Ce-doped Mn/TiO_2 catalysts for the low-temperature SCR of NOx under oxygen-rich conditions, J. Catal. 325 (2015) 145–155.

[37] B. Bai, H. Arandiyan, J. Li, Comparison of the performance for oxidation of formaldehyde onnano-Co_3O_4, 2D-Co_3O_4, and 3D-Co_3O_4 catalysts, Appl. Catal. B: Environ. 142–143 (2013) 677–683.

[38] P.A. Kumar, M.D. Tanwar, N. Russo, R. Pirone, D. Fino, Synthesis and catalytic properties of CeO_2 and Co/CeO_2 nanofibres for diesel soot combustion, Catal. Today 184 (2012) 279–287.

[39] N. Russo, S. Furfori, D. Fino, G. Saracco, V. Specchia, Lanthanum cobaltite catalysts for diesel soot combustion, Appl. Catal. B: Environ. 83 (2008) 85–95.

[40] G.M. Veith, J. Nanda, L.H. Delmau, N.J. Dudney, Influence of lithium salts on the discharge chemistry of Li–air cells, J. Phys. Chem. Lett. 3 (2012) 1242–1247.

[41] J. Li, N. Yan, Z. Qu, S. Qiao, S. Yang, Y. Guo, P. Liu, J. Jia, Catalytic oxidation of elemental mercury over the modified catalyst Mn/α-Al_2O_3 at lower temperatures, Environ. Sci. Technol. 44 (2010) 426–431.

[42] H. Li, S. Wu, L. Li, J. Wang, W. Ma, K. Shih, CuO–CeO_2/TiO_2 catalyst for simultaneous NO reduction and Hg^0 oxidation at low temperatures, Catal. Sci. Technol. 5 (2015) 5129–5138.

[43] H. Li, C.-Y. Wu, Y. Li, J. Zhang, CeO_2-TiO_2 catalysts for catalytic oxidation of elemental mercury in low-rank coal combustion flue gas, Environ. Sci. Technol. 45 (2011) 7394–7400.

[44] Y. Xie, C. Li, L. Zhao, J. Zhang, G. Zenga, X. Zhang, W. Zhang, S. Tao, Experimental study on Hg^0 removal from flue gas over columnar MnO_x-CeO_2/activated coke, Appl. Surf. Sci. 333 (2015) 59–67.

[45] Q. Wan, L. Duan, K. He, J. Li, Removal of gaseous elemental mercury over a

CeO_2–WO_3/TiO_2 nanocomposite in simulated coal-fired flue gas, Chem. Eng. J. 170 (2011) 512–517.

[46] S. Yang, W. Zhu, Z. Jiang, Z. Chen, J. Wang, The surface properties and the activities in catalytic wet air oxidation over CeO_2–TiO_2 catalysts, Appl. Surf. Sci. 252 (2006) 8499–8505.

[47] Y. Jiang, Z. Xing, X. Wang, S. Huang, X. Wang, Q. Liu, Activity and characterization of a Ce–W–Ti oxide catalyst prepared by a single step sol–gel method for selective catalytic reduction of NO with NH_3, Fuel 151 (2015) 124–129.

[48] P. Ning, Z. Song, H. Li, Q. Zhang, X. Liu, J. Zhang, X. Tang, Z. Huang, Selective catalytic reduction of NO with NH_3 over CeO_2–ZrO_2–WO_3 catalysts prepared by different methods, Appl. Surf. Sci. 332 (2015) 130–137.

[49] X. Zhang, B. Shen, F. Shen, X. Zhang, M. Si, P. Yuan, The behavior of the manganese-cerium loaded metal-organic framework in elemental mercury and NO removal from flue gas, Chem. Eng. J. 326 (2017) 551–560.

[50] T. Cai, H. Huang, W. Deng, Q. Dai, W. Liu, X. Wang, Catalytic combustion of 1,2-dichlorobenzene at low temperature over Mn-modified Co_3O_4 catalysts, Appl. Catal. B: Environ. 166–167 (2015) 393–405.

[51] Z. Tian, P.H.T. Ngamou, V. Vannier, K. Kohse-Höinghaus, N. Bahlawane, Catalytic oxidation of VOCs over mixed Co–Mn oxides, Appl. Catal. B: Environ. 117–118 (2012) 125–134.

[52] M. Konsolakis, M. Sgourakis, S.A.C. Carabineiro, Surface and redox properties of cobalt–ceria binary oxides: on the effect of Co content and pretreatment conditions, Appl. Surf. Sci. 341 (2015) 48–54.

[53] N.D. Hutson, B.C. Attwood, K.G. Scheckel, XAS and XPS characterization of mercury binding on brominated activated carbon, Environ. Sci. Technol. 41 (2007) 1747–1752.

[54] R. Jin, Y. Liu, Z. Wu, H. Wang, T. Gu, Low-temperature selective catalytic reduction of NO with NH_3 over Mn-Ce oxides supported on TiO_2 and Al_2O_3: a comparative study, Chemosphere 78 (2010) 1160–1166.

[55] G. Qi, R.T. Yang, R. Chang, MnO_x-CeO_2 mixed oxides prepared by co-precipitation for selective catalytic reduction of NO with NH_3 at low temperatures, Appl. Catal. B: Environ. 51 (2004) 93–106.

[56] F. Cao, J. Xiang, S. Su, P. Wang, L. Sun, S. Hu, S. Lei, The activity and characterization of MnO_x–CeO_2–ZrO_2/γ-Al_2O_3 catalysts for low temperature selective catalytic reduction of NO with NH_3, Chem. Eng. J. 243 (2014) 347–354.

[57] H. Fu, X. Wang, H. Wu, Y. Yin, J. Chen, Heterogeneous uptake and oxidation of SO_2 on iron oxides, J. Chem. Phys. C 111 (2007) 6077–6085.

[58] J. García-Martínez, D. Cazorla-Amorós, A. Linares-Solano, SO_2-Faujasite interaction: a study by in situ FTIR and thermogravimetry, Langmuir 18 (2002) 9778–9782.

[59] A. Bueno-López, K. Krishna, M. Makkee, J.A. Moulijn, Enhanced soot oxidation by lattice oxygen via La^{3+}-doped CeO_2, J. Catal. 230 (2005) 237–248.

[60] H. Li, Y. Li, C. Wu, J. Zhang, Oxidation and capture of elemental mercury over SiO_2–TiO_2–V_2O_5 catalysts in simulated low-rank coal combustion flue gas, Chem. Eng. J. 169 (2011) 186–193.

[61] Y. Xu, Q. Zhong, X. Liu, Elemental mercury oxidation and adsorption on magnesite powder modified by Mn at low temperature, J. Hazard. Mater. 283 (2015) 252–259.

[62] M. Casapu, O. Kröcher, M. Elsener, Screening of doped MnO_x–CeO_2 catalysts for low-temperature NO-SCR, Appl. Catal. B: Environ. 88 (2009) 413–419.

[63] W. Xu, H. He, Y. Yu, Deactivation of a Ce/TiO_2 catalyst by SO_2 in the selective catalytic reduction of NO by NH_3, J. Chem. Phys. C 113 (2009) 4426–4432.

[64] Y. Li, P.D. Murphy, C. Wu, K. Powers, J.C.J. Bonzongo, Development of silica/vanadia/titania catalysts for removal of elemental mercury from coal combustion flue gas, Environ. Sci. Technol. 42 (2008) 5304–5309.

[65] S. Niksa, N. Fujiwara, A predictive mechanism for mercury oxidation on selective catalytic reduction catalysts under coal-derived flue gas, J. Air Waste Manage. 55 (2005) 1866–1875.

[66] Y. Shi, S. Chen, H. Sun, Y. Shu, X. Quan, Low-temperature selective catalytic reduction of NO_x with NH_3 over hierarchically macro-mesoporous Mn/TiO_2, Catal. Commun. 42 (2013) 10–13.

[67] C. He, B. Shen, F. Li, Effects of flue gas components on removal of elemental mercury over Ce-MnO_x/Ti-PILCs, J. Hazard. Mater. 304 (2016) 10–17.

[68] R. Grabowski, S. Pietrzyk, J. Słoczyński, F. Genser, K. Wcisło, B. Grzybowska-Świerkosz, Kinetics of the propane oxidative dehydrogenation on vanadia/titania catalysts from steady-state and transient experiments, Appl. Catal. A: Gen. 232 (2002) 277–288.

[69] J. Yang, Y. Zhao, J. Zhang, C. Zheng, Regenerable cobalt oxide loaded magnetosphere catalyst from fly ash for mercury removal in coal combustion flue gas, Environ. Sci. Technol. 48 (2014) 14837–14843.

[70] A.A. Presto, E.J. Granite, Survey of catalysts for oxidation of mercury in flue gas, Environ. Sci. Technol. 40 (2006) 5601–5609.

[71] G. Marbán, T. Valdés-Solís, A.B. Fuertes, Mechanism of low-temperature selective catalytic reduction of NO with NH_3 over carbon-supported Mn_3O_4 role of surface NH_3 species: SCR mechanism, J. Catal. 226 (2004) 138–155.

[72] M. Kang, E.D. Park, J.M. Kim, J.E. Yie, Cu–Mn mixed oxides for low temperature NO reduction with NH_3, Catal. Today 111 (2006) 236–241.

[73] Y.H. Li, C.W. Lee, B.K. Gullett, Importance of activated carbon's oxygen surface functional groups on elemental mercury adsorption, Fuel 82 (2003) 451–457.